

**New paleointensity data from Aniakchak volcano,
Alaska, USA**

Geoffrey Cromwell^{1,2} and Yiming Zhang^{1,3}

¹Occidental College, Los Angeles, CA, USA

²Current Address: U.S. Geological Survey, California Water Science Center, Santa Maria, CA, USA

³Current Address: University of California Berkeley, Berkeley, CA, USA

Key Points:

- We report the first set of absolute paleointensity data from Aniakchak volcano, Alaska, USA.
- Glassy volcanic material yield high-quality results and were evaluated using strict-selection criteria
- The new data fill in a gap of Holocene-age absolute paleointensity records from mid- to high-latitudes in North America

14 **Abstract**

15 This study presents the first set of Holocene-age, high-quality absolute paleointensity data
 16 from Alaska, USA. Existing paleointensity data for the Holocene are generally located
 17 at mid-northern latitudes in North America, Europe, the Middle East, and eastern Asia.
 18 Relatively few data are from the Alaska region. IZZI-modified paleointensity experiments
 19 were conducted on glassy volcanic materials from Aniakchak volcano, a mid- to high-
 20 latitude composite volcano on the Alaska-Aleutian arc.

21 The CCRIT selection criteria were applied to the paleointensity results. A total
 22 of 30 specimens from six samples with estimated ages ranging from 1931 C.E. to 2,300
 23 years before present passed all selection criteria. The sample-mean paleointensities ranged
 24 from about 49 to 68 microTesla (μ T). The sample-mean paleointensity results are com-
 25 parable to modeled intensities, however all except for one sample-mean paleointensity
 26 are lower than those predicted by geomagnetic field models. The paleointensity estimate
 27 for the historic 1931 C.E. eruption was about 15 μ T greater than the expected field strength.
 28 This overestimate may result from unrecognized alteration or non-ideal remanence car-
 29 riers in this sample. Further evaluation of samples from the 1931 C.E. eruption using
 30 a Bayesian estimation method resulted in a paleointensity estimate that encompasses the
 31 historical field strength within uncertainty. These new paleointensity results are a val-
 32 uable contribution to the mid- to high-northern latitude paleomagnetic dataset. Incor-
 33 poration of these data into future geomagnetic field models will improve the predictions
 34 of geomagnetic field behavior in the Alaska region.

35 **1 Introduction**

36 Reconstructing the Holocene evolution of Earth's magnetic field is important for
 37 understanding geodynamo processes in Earth's core, for studying long-term solar-terrestrial
 38 relationships, and for providing useful age constraints for archeological and stratigraphic
 39 units. Currently there are several observation-based, continuous global geomagnetic field
 40 models (Constable et al., 2016; Korte et al., 2009; Korte & Constable, 2011; Korte et al.,
 41 2011; Pavón-Carrasco et al., 2014; Nilsson et al., 2014) that have various reconstructions
 42 and predictions of paleodirection and absolute paleointensity using historic measurements
 43 of the geomagnetic field and paleomagnetic data from archeomagnetic, volcanic, and sed-
 44 imentary materials. Depending on the availability of spatially and temporally distributed
 45 reliable paleomagnetic data, the accuracy and resolution of different models of the past
 46 geomagnetic field can vary. Currently the majority of the Holocene archeomagnetic and
 47 volcanic paleointensity data come from mid-northern latitudes (30°N to about 50°N) in
 48 North America, Europe, the Middle East, and eastern Asia (Brown, Donadini, Korte,
 49 et al., 2015; Brown, Donadini, Nilsson, et al., 2015), biasing the models toward better
 50 resolution in these regions and lower resolutions in the higher latitudes and in the south-
 51 ern hemisphere. To improve future geomagnetic field models, it is essential to add more
 52 high-quality paleomagnetic data from areas with few current data points.

53 An under-represented region in the current paleomagnetic database is Alaska, es-
 54 pecially along the volcanically active Alaska-Aleutian arc. Previous paleomagnetic stud-
 55 ies in Alaska have mostly focused on tectonic questions on mainland Alaska (Packer &
 56 Stone, 1974; Hillhouse & Grommé, 1980; Thrupp & Coe, 1986; Stamatakos et al., 2001),
 57 or paleosecular variation studies on volcanoes along the Alaska-Aleutian arc (Stone &
 58 Packer, 1979; Bingham & Stone, 1972; Stone & Layer, 2006) and on Nunivak Island (Coe
 59 et al., 2000; Johnson et al., 2008). Paleointensity records from Alaska are limited, espe-
 60 cially absolute paleointensity records. Previous studies focused on determining the rel-
 61 ative paleointensity records from sediment cores with the purpose of better constrain-
 62 ing the regional chronostratigraphy of the western Arctic (Barletta et al., 2008; Lisé-Pronovost
 63 et al., 2009). Stone and Layer (2006) conducted absolute paleointensity experiments us-
 64 ing Thellier-Coe method (Coe, 1967) on lava flows from the Aleutian Islands. However,

only two samples from a *ca.* 2 Ma lava flow and one sample from a *ca.* 50 ka lava flow yielded acceptable paleointensity results. An evaluation of the efficacy of paleointensity experiments on pyroclastic-flow material from the historical 1912 C.E. Novarupta volcano was conducted by Bowles et al. (2015). Sparse temporal coverage, and low success rate for absolute paleointensity records have limited systematic interpretation of the geomagnetic field behavior over the Alaska-Aleutian arc region.

Nevertheless, volcanoes of the Alaska-Aleutian arc are promising targets for northern mid- to high-latitude paleointensity investigations because of the active volcanism along the arc, availability of detailed geologic maps, and the preservation of fresh, glassy volcanic materials which can be faithful paleointensity recorders (Cromwell, Tauxe, & Halldórsson, 2015; Cromwell, Tauxe, Staudigel, & Ron, 2015; Cromwell et al., 2018). Aniakchak volcano, an active Pleistocene-Holocene composite volcano, is one such target (Figure 1). The volcano has undergone at least one caldera-forming eruption in post-glacial time and last erupted in 1931 C.E. (Bacon et al., 2014). Aniakchak volcano contains glassy volcanic materials and has an established stratigraphic record that is calibrated based on ^{14}C radiocarbon geochronology constraints from organic materials within or between eruptive materials (Bacon et al., 2014). To date, no paleomagnetic studies have been conducted on Aniakchak volcano.

Glassy volcanic materials from Aniakchak can be ideal targets for paleointensity experiments because single domain stable magnetic minerals tend to form during rapid cooling and often yield ideal paleointensity behaviors (Tauxe & Staudigel, 2004; Dunlop, 2005). A previous paleointensity study successfully obtained high-quality paleointensity estimates using submarine basaltic glass as old as 92 Ma (Tauxe & Staudigel, 2004). More recent paleointensity studies on young (centuries to tens of thousands of years), fresh, glassy volcanic materials, formed from sub-aerial and sub-glacial eruptions, have accurately recovered geomagnetic field strengths that match with modeling results (Cromwell, Tauxe, & Halldórsson, 2015; Cromwell, Tauxe, Staudigel, & Ron, 2015; Cai et al., 2017; Cromwell et al., 2018). In this study, we conduct IZZI-modified paleointensity experiments (Tauxe & Kent, 2004) on glassy volcanic materials from Aniakchak volcano. Our data add to the observational records of the geomagnetic field strength at mid- to high-northern latitudes in Alaska during the Holocene.

2 Geologic Setting

The Alaska-Aleutian arc is an active chain of volcanoes that formed in the Eocene (Jicha et al., 2006) as a result of subduction of the Pacific Plate under the North American Plate. Aniakchak volcano (located at approximately 56.9 °N, -158.2 °E) is a Pleistocene-Holocene composite volcano located in the eastern part of the Alaska-Aleutian arc on the Alaska Peninsula, about 670 km southwest of Anchorage, Alaska (Figure 1). Aniakchak has been an active volcano since the last glacial period, having experienced multiple sub-Plinian to Plinian eruptions. The earliest Holocene Aniakchak eruption has been dated with radiocarbon method to have occurred between *ca.* 9,500 and 7,000 years ago before present (yrs B.P.; VanderHoek (2009)), and the latest eruption was a sub-Plinian eruption in 1931 C.E.

Aniakchak volcano has been the subject of several geologic investigations, the most comprehensive one being a report on the postglacial eruption history, geochemistry and recent seismicity of the volcano by Bacon et al. (2014). Bacon et al. (2014) built upon previous investigations of the eruptive history of the volcano (Miller & Smith, 1977, 1987; C. Neal et al., 1992; VanderHoek & Myron, 2004; VanderHoek, 2009), specific eruptive and geologic events (Begét et al., 1992; McGimsey et al., 1994), potential volcanic hazards (C. A. Neal et al., 2001), and the geochemistry, petrology and magma evolution of the volcano (George, 2004; Dreher et al., 2005; Symonds et al., 2003). A study by Pearce et al. (2017) uses tephra from a radiocarbon-dated Aniakchak eruption to constrain the

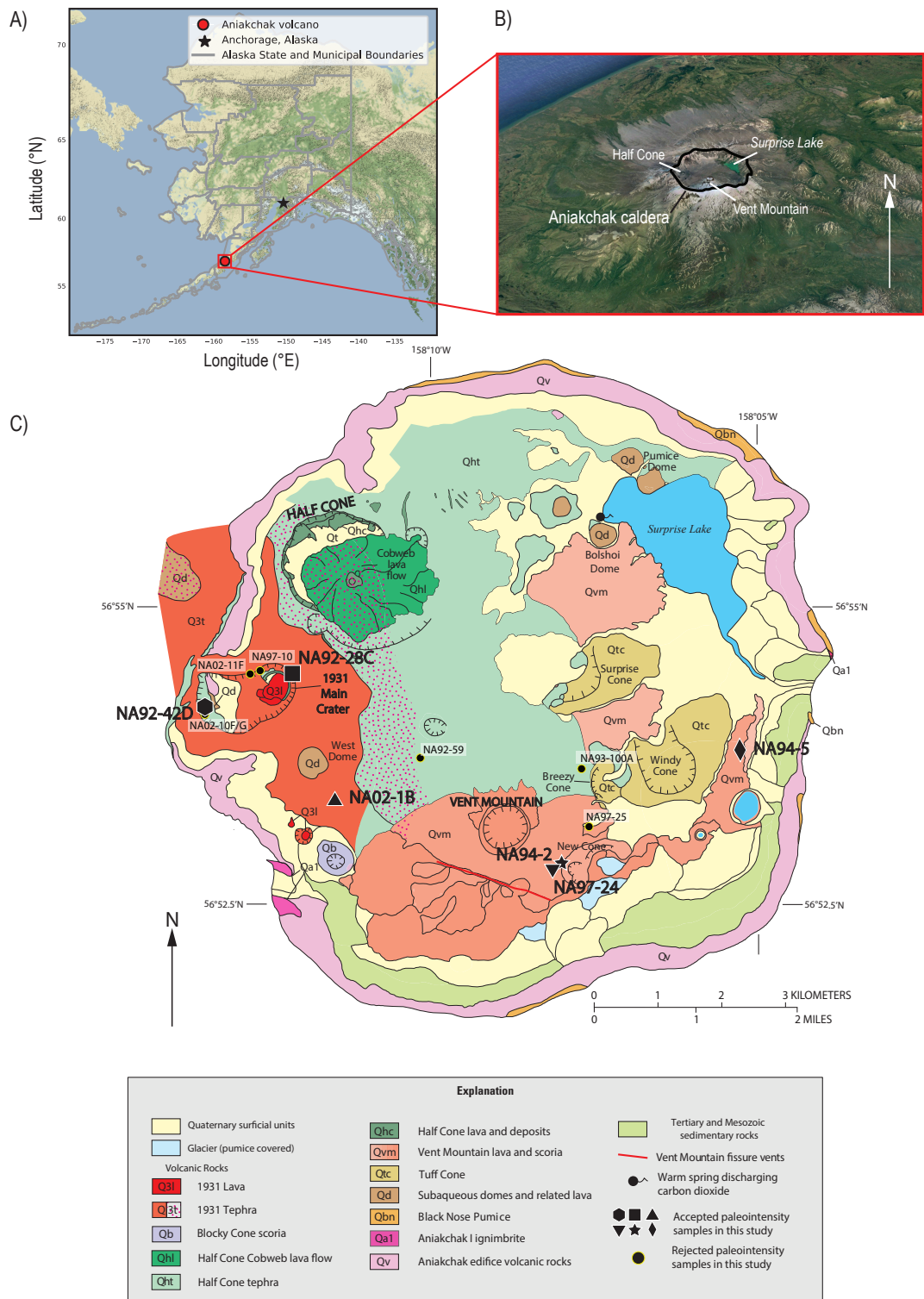


Figure 1. Regional setting of Aniakchak volcano. A) Location of Aniakchak volcano with respect to the State of Alaska, USA, the city of Anchorage, and municipal boundaries; B) perspective view of Aniakchak volcano (GoogleEarth imagery); C) Geologic map of Aniakchak caldera with locations of paleointensity sample used in this study, modified from Bacon et al. (2014).

116 chronology of submarine sediments. The earliest reports specific to Aniakchak were by
 117 Smith (1925), who published the first geologic map of the crater, and by Hubbard (1931),
 118 who visited Aniakchak before and after the historical 1931 C.E. eruption. This inves-
 119 tigation of paleointensity will be the first paleomagnetic investigation of Aniakchak vol-
 120 cano.

121 Aniakchak volcano has had two major postglacial eruptions (Miller & Smith, 1987).
 122 Aniakchak I is the oldest known eruption and the age of its andesite ignimbrite deposits
 123 has been bracketed by the timing of deglaciation around 9,500 yrs B.P. and ^{14}C ages of
 124 *ca.* 7,000 yrs B.P. of organic materials beneath stratigraphically younger pumice-fall de-
 125 posits (VanderHoek, 2009). The other major eruption, named Aniakchak II, is estimated
 126 to have occurred *ca.* $3,430 \pm 70$ yrs B.P. based on ^{14}C ages of charcoal within an ignimbrite
 127 emplaced during the event (Miller & Smith, 1987; Bacon et al., 2014). The Aniakchak
 128 II event formed the outer boundary of the present-day Aniakchak caldera (Figure 1). Mul-
 129 tiple following eruptive events after the Aniakchack II eruption are summarized in de-
 130 tail by Bacon et al. (2014) and illustrated in Figure 1. The post-Aniakchak II record is
 131 complicated by a caldera lake having been present for part of this period, and little in-
 132 formation is known about the earliest postcaldera materials prior to the emplacement
 133 of the dacite domes (unit Qd; Figure 1; Bacon et al. (2014)). From the oldest to youngest,
 134 Bacon et al. (2014) describe the post-Aniakchak II geologic history to consist of subaque-
 135 ous lava effusions forming dacite domes and related lava (Qd), catastrophic draining of
 136 the caldera lake, subsequent hydromagmatic eruptions forming the tuff cones (Qtc), later
 137 effusive and explosive eruptions that resulted in the formation of lava and scoria from
 138 Vent Mountain (Qvm), Half Cone (Qhc, Qht, Qhl), and scoria from Blocky Cone (Qb).
 139 Finally, the 1931 C.E. eruption of tephra (Q3t) and lava flows (Q3l). Some of the post-
 140 Aniakchack II eruptive materials are overlain by glaciers and surficial deposits.

141 3 Sample Collection

142 Unoriented hand-samples were collected by the U.S. Geological Survey (USGS) Alaska
 143 Volcano Observatory in Anchorage, Alaska as part of an effort to document the erup-
 144 tion history of Aniakchack volcano, which included conducting ^{14}C radiometric age dat-
 145 ing of organic materials to provide chronological control for the stratigraphic sections
 146 of the volcano, and conducting detailed geochemical analyses to document the magmatic
 147 processes associated with Aniakchak eruptions (Bacon et al., 2014). For this study, thir-
 148 teen samples of those collected by the USGS were acquired for paleointensity experiments
 149 from the Geologic Materials Center (2015) in Anchorage, Alaska. Sample location in-
 150 formation, descriptions, geologic unit assignments, and age estimates are listed in Ta-
 151 ble 1. Age estimates for each sample were interpreted for this study, all other informa-
 152 tion in Table 1 was previously published in Bacon et al. (2014) or available from the Geologic
 153 Materials Center (2015). The original sample names used by Bacon et al. (2014) and the
 154 Geologic Materials Center (2015) are retained in this study. The samples included in this
 155 study are post-Aniakchak II eruptive materials and range in age from *ca.* 2,300 yrs B.P.
 156 to 1931 C.E.

157 3.1 Stratigraphy and Age Constraints

158 Age constraints for the samples included in this study were interpreted based on
 159 sample descriptions and stratigraphic and radiometric age constraints reported by Bacon
 160 et al. (2014), or summarized therein. The estimated ages of volcanic deposits in Aniakchak
 161 volcano were acquired through ^{14}C dating on organic materials found in between tephra
 162 layers and lava flows in addition to stratigraphic relationships (Bacon et al., 2014). The
 163 interpreted age estimates for each sample are based on the geologic unit of each sample
 164 (Table 1); unit assignments for all samples are from Bacon et al. (2014), except for sam-
 165 ples NA02-10F and NA02-11F which are interpreted for this study based on their loca-

166 tion information and descriptions. Additional evaluation of the geochemical data of Bacon
 167 et al. (2014) (Figure 2) may help constrain the age of selected samples. Ages reported
 168 by Bacon et al. (2014), and used in this study, are given in radiocarbon years before 1950
 169 C.E. In this section we briefly describe the location, geologic unit, and estimated ages
 170 for each sample used in our paleointensity experiment.

171 *3.1.1 Subaqueous Domes (unit Qd)*

172 Samples NA92-42D and NA02-10G were collected from the subaqueous domes and
 173 related lava flows (unit Qd; Figure 1) which has an estimated age range of 2,3001,860
 174 yrs B.P. (Table 1). The subaqueous domes are the oldest known products of post-Aniakchak
 175 II caldera-forming volcanism that were effused in an ancient caldera lake, of which mod-
 176 ern Surprise Lake is a remnant (Figure 1; Bacon et al. (2014)). The ancestral caldera
 177 lake was estimated to have catastrophically drained prior to $1,860 \pm 30$ yr B.P. based on
 178 radiocarbon ages on wood from above sediment near the Aniakchak River mouth of $1,860 \pm 30$
 179 yr B.P. (VanderHoek & Myron, 2004; Bacon et al., 2014)), thereby providing a minimum
 180 age constraint for emplacement of the subaqueous domes. A ca. 2,300 yr B.P. pumice
 181 fall (derived from a radiocarbon age of $2,300 \pm 80$ yr B.P. from Bacon et al. (2014)) is ten-
 182 tatively considered by Bacon et al. (2014) to have preceded, or to be contemporaneous
 183 with the emplacement of the subaqueous domes, thereby providing a maximum age con-
 184 straint for the subaqueous domes.

185 *3.1.2 Tuff Cone (unit Qtc)*

186 Sample NA94-5 was collected from Tuff Cone (unit Qtc; Figure 1), which has an
 187 estimated age range of 900 to 1,860 yrs B.P. (Table 1; Bacon et al. (2014)). Radiocar-
 188 bon dating of a soil above a tephra with Surprise Cone-like chemistry yielded a weighted
 189 mean age of 900 ± 80 yr B.P. (Bacon et al., 2014), which is interpreted to provide a min-
 190 imum age constraint for the emplacement of the Tuff Cone unit. The tuff cones are thought
 191 to postdate catastrophic draining of the ancestral caldera lake ($1,860 \pm 30$ yr B.P.;VanderHoek
 192 and Myron (2004); Bacon et al. (2014)) to their approximate elevation in the caldera.
 193 This age is interpreted as a maximum age constraint for the emplacement of the Tuff Cone
 194 unit. We therefore assign an age range of sample NA94-5 to be between 900 and 1,860
 195 yrs B.P.

196 The geochemical composition of sample NA94-5 may further constrain its emplace-
 197 ment age. Sample NA94-5 was collected east of Windy Cone and has a basaltic andesite
 198 geochemistry attribute (Figure 2) that resembles the mafic eruption material of the Tuff
 199 Cone unit. The range of total alkaline silicate (TAS) compositions for all Tuff Cone sam-
 200 ples collected by Bacon et al. (2014) (Figure 2) indicates that there might have been a
 201 magmatic evolution of material from more felsic to more mafic compositions, perhaps
 202 similar to what was observed for the duration of the Aniakchak II caldera-forming erup-
 203 tion (Bacon et al., 2014). If magmatic evolution occurred during the development of the
 204 Tuff Cones, the low-silica/high-mafic composition of NA94-5 could indicate that it was
 205 emplaced near the end of the Tuff Cone eruptive period and could be closer to the younger
 206 radiocarbon age constraint of 900 ± 80 yr B.P. (Bacon et al., 2014). However, without di-
 207 rect geochronologic constraints on the sample, we consider the age uncertainty of this
 208 sample to be 9001,860 yr B.P.

209 *3.1.3 Vent Mountain (unit Qvm)*

210 Samples NA97-25, NA94-2, NA97-24, and NA93-100A were collected from the Vent
 211 Mountain lava and scoria (unit Qvm; Figure 1) and were assigned ages between 400 ± 30
 212 and 900 yrs B.P. (Table 1). The Vent Mountain scoria and spatter cone rises 440530 me-
 213 ters above the Aniakchak caldera floor and is the most prominent topographic feature
 214 within the caldera (Bacon et al., 2014). Lava flows and other eruptive materials of this

unit were sourced from Vent Mountain itself, from fissures on the mountain flank, and from the nearby New Cone (Figure 1). Materials from Vent Mountain and New Cone are stratigraphically above the Tuff Cones unit (which has a minimum radiocarbon age of 900 ± 80 yr B.P.; Bacon et al. (2014)), below the 1931 C.E. eruption, and are interbedded with eruptive materials from Half Cone (Bacon et al., 2014).

Samples NA94-2 and NA97-24 were collected from the rim of New Cone, and sample NA97-25 was described by Bacon et al. (2014) to have been sampled from a lava flow possibly related to New Cone (Table 1). Bacon et al. (2014) determined a radiocarbon mean age of 400 ± 30 yr B.P. for tephra interpreted to have originated from New Cone based on multiple *ca.* 400 yr B.P. radiocarbon ages of wood and organic sediments associated with these tephra deposits. We therefore assign this weighted radiocarbon mean age of 400 ± 30 yr B.P. to samples NA94-2, NA97-24, and NA97-25.

Sample NA93-100A was reported to have been collected from a Vent Mountain "...lava younger than tuff cones, at base of tephra section" (Appendix Table B1 in Bacon et al. (2014)). We interpret this description to mean that the lava flow is the oldest Vent Mountain lava in the schematic composite stratigraphic section of Bacon et al. (2014) which has a minimum age of 840 ± 30 yr B.P. and a maximum age of 900 ± 80 yr B.P. We therefore assign an age range of 840–900 yrs B.P. to sample NA93-100A.

3.1.4 Half Cone (units Qht and Qhc)

Samples NA92-59, NA92-28C, and NA02-10F were collected from the Half Cone tephra (unit Qht; Figure 1), and sample NA02-11F was collected from the Half Cone Cobweb lava (unit Qhc). Unit assignments for NA02-10F and NA02-11F were interpreted for this study based on their location information and descriptions (Table 1). These samples were not included in the chemical analysis of Aniakchak volcano by Bacon et al. (2014). Half Cone today is a remnant of an andesitedacite composite edifice whose southeastern part had been destroyed by explosive eruptions late in its eruptive life. Volcanic materials from Half Cone generally consist of pumice-fall deposits, pyroclastic-flow deposits, tephra deposits, and dacitic lava flows. Materials from Half Cone are generally interbedded with those from Vent Mountain. Radiocarbon age dates of organic materials associated with Half Cone deposits range from 380 ± 50 to 840 ± 40 yrs B.P (Bacon et al., 2014). Late-eruption fall deposits and the Cobweb lava flow (the final eruptive product of Half Cone) are stratigraphically above the dated material and postdate those eruptive events.

Sample NA92-59 is from agglutinate materials sampled at the north base of Vent Mountain. This sample is described to be from a late-erupted Half Cone pyroclastic fall layer stratigraphically above the Brown Pumice fall and the underlying Pink Pumice fall (380 ± 50 yr B.P. radiocarbon age; Bacon et al. (2014)). The Brown Pumice Fall and Pink Pumice Fall were emplaced by a series of Plinian eruptions that produced widespread pumice falls and destroyed much of the original Half Cone edifice (Bacon et al., 2014). Sample NA92-59 has a SiO_2 weight percent of 59.49, which is within the reported range of the Brown Pumice fall of about 58–61 weight percent (Bacon et al., 2014). The geochemistry data is consistent with the stratigraphic interpretation that this sample is related to the eruptive materials of the Half Cone pumice falls, we therefore assign the Pink Pumice Fall radiocarbon age of 380 ± 50 yr B.P. to this sample.

Sample NA92-28C is agglutinate material sampled from the 1931 main crater wall (Table 1). Based on the sample descriptions and location of this sample, it is likely that sample NA92-28C was collected from the *ca.* 400 yrs B.P. Half Cone agglutinate exposed in the north wall of the 1931 Main Crater (Bacon et al., 2014). Sample NA02-10F has a similar sample description and location as sample NA92-28C. Therefore, we interpret that sample NA02-10F was collected from the same agglutinate exposure. We assume that the *ca.* 400 yrs B.P. age ascribed by (Bacon et al., 2014) for this exposure is derived from the 380 ± 50 yr B.P. radiocarbon age for the Half Cone Pink Pumice Fall which is

one of the most areally extensive units of Half Cone *ca.* 400 yr B.P. Plinian eruptions. We therefore assign an age of 380 ± 50 yr B.P. to both samples NA92-28C and NA02-10F.

Sample NA02-11F consists of welded volcaniclastic material collected from the north wall of the 1931 Main Crater. The welded agglutinate description for this sample is consistent with what Bacon et al. (2014) describes as partly welded or indurated coarse pyroclastic-flow material at the base of the 1931 Main Crater exposure. We interpret that sample NA02-11F was collected from this basal material. The basal unit is stratigraphically overlain by pumice-fall deposits in the 1931 Main Crater exposure, which Bacon et al. (2014) indicate may be correlative with the lower and upper light pumice that have weighted mean radiocarbon ages of 840 ± 40 and 570 ± 40 yrs B.P. respectively. Based on the above interpretations, sample NA02-11F is likely older than the lower light pumice and we therefore assign an age of $<840 \pm 40$ yrs. B.P. to the sample (Table 1).

3.1.5 1931 C.E. Eruption (units Q31t and Q31l)

Samples NA02-1B and NA97-10 were collected from material emplaced during the 1931 C.E. eruption. Sample NA02-1B is a scoriaceous material from the 1931 Tephra (unit Q3t), and sample NA02-1B is from a spatter-fed lava flow from the 1931 Lava (unit Q3l). The 1931 C.E. Aniakchak eruption was a 6-week-long eruption that began with relatively silica-rich daciterhyodacite magma and ended with relatively silica-poor basaltic andesite magma (Nicholson et al., 2011). Within and near the caldera, the 1931 deposit consists of pumiceous fall deposits (Nicholson et al., 2011). A 50100-cm-thick stratified deposit of agglutinated basaltic-andesite lapilli and minor scoria bomb partly mantles the north and east wall of the Main Crater (Bacon et al., 2014). A vesicular basaltic andesite lava covers much of the floor of the Main Crater and is mantled by spatter agglutinate.

4 Methods

4.1 Paleointensity Experiment

Specimens were selected based on their visual and textural appearance for the paleointensity experiment (Figure 3). The glassy textures shown in all specimens in Figure 3 here are indicative of rapid cooling, which tends to promote the formation of single domain magnetic carriers that often succeed in paleointensity experiments (Tauxe & Staudigel, 2004). Specimens chosen for the paleointensity experiment have glassy textures and have a minimum magnetic moment of $1.0E^{-7}$ Am 2 . Specimens were wrapped in non-magnetic glass microfiber filters and glued inside 12 mm-diameter glass vials with potassium silicate. All glass vials were treated with a 600°C heating in a zero-field to remove any remanent magnetization; vials used in the paleointensity experiment had a resulting magnetic moments smaller than $1.0E^{-10}$ Am 2 . Between five and nine specimens were prepared for each sample (Table 1).

Paleointensity experiments were conducted at the paleomagnetic laboratory at Scripps Institution of Oceanography at the University of California San Diego. All experiments were conducted in a shielded room which had a background magnetic field less than 400 nanoTesla (nT). The IZZI-modified double heating protocol was used for the paleointensity experiment (Yu et al., 2004) using custom-built ovens. For zero-field heating steps the background magnetic field in the ovens was reduced to less than 5 nT. A laboratory field of 35 μ T was applied during in-field heating steps along the Z-axis of the oven, parallel to the long axis of glass vials. Specimens were treated up to 600°C or until at least 95% of the natural remanent magnetization (NRM) was removed. Partial thermal remanent magnetization (pTRM) checks for alterations were applied at every other temperature step. NRM and pTRM measurements were performed using a 2G Cryogenic Magnetometer.

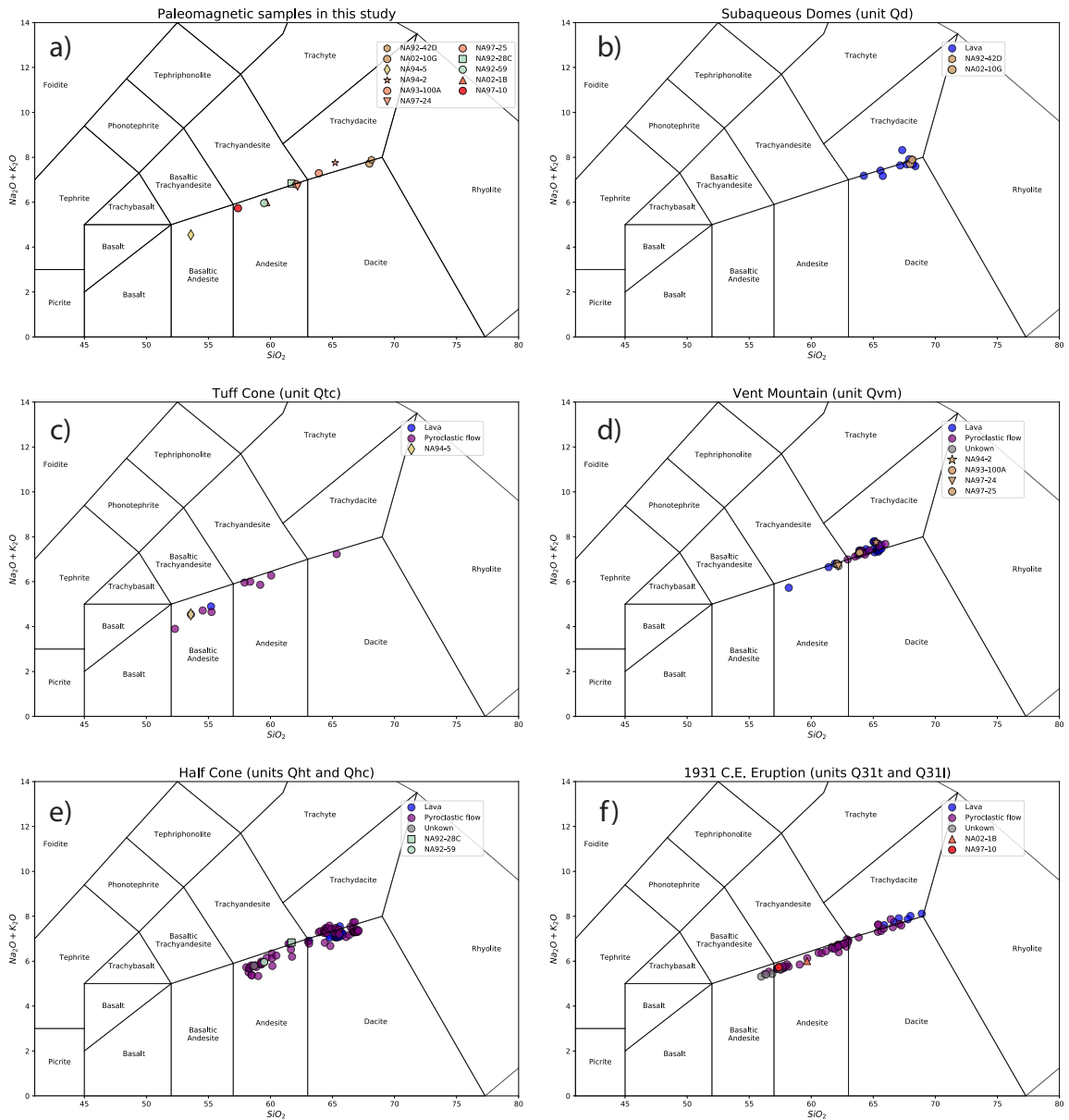


Figure 2. Total alkaline silica (TAS) plots for all Aniakchak units associated with this study. Plot a) includes all samples used in this study except for sample NA02-10F. Plots b to f show compilations of TAS measurements in Appendix Table B1 in Bacon et al. (2014) for all samples related to units of interests in this study.

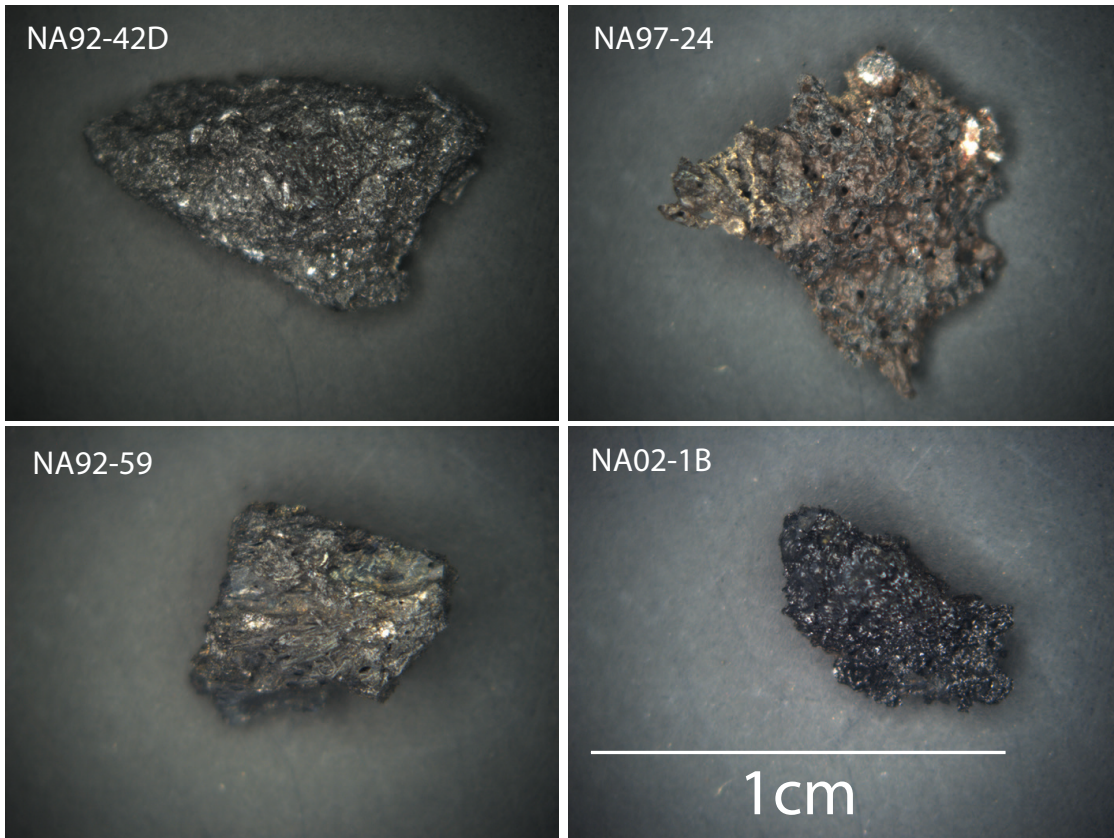


Figure 3. Binocular images of representative glassy volcanic materials that are sister specimens with those used for paleointensity experiments in this study. All images share the same scale as shown by the 1-centimeter scale bar in the image for sample NA02-1B.

315 **4.2 Selection Criteria**

316 Data interpretation was performed using the Thellier GUI Auto Interpreter (Shaar
 317 & Tauxe, 2013), part of the PmagPy software package (Tauxe et al., 2016), using the
 318 CCRIT selection criteria (Cromwell, Tauxe, Staudigel, & Ron, 2015). CCRIT was de-
 319 signed to limit the selected specimen results to be those containing only a single direc-
 320 tional magnetic component and near-linear slopes in NRM/TRM Arai plots (Arai, 1963).
 321 This criteria has been useful in filtering out non-ideal specimens, such as those with poor
 322 Arai behavior and those producing poor within-sample paleointensity dispersion. Specimen-
 323 and sample-level requirements of CCRIT are listed in Table 2, and brief descriptions are
 324 provided below (more detailed explanations of each criterium are presented in Paterson
 325 et al. (2014). β is the standard deviation of the slope of selected data points normalized
 326 by the absolute value of the slope. *SCAT* is a Boolean based on the value of β and eval-
 327 uates the degree of scatter of the selected data points about the best fit slope. Here the
 328 threshold of β is set at 0.1. *FRAC* measures the fraction of the NRM used in calculat-
 329 ing the best fit line. *Gap Max* sets the maximum gap between two consecutive NRM/TRM
 330 points on Arai plot. *MAD* is the maximum angle of deviation representing the scatter
 331 of selected through demagnetization procedures about the unanchored best fit line. *DANG*
 332 measures the angle between the best fit line and the line determined by the center of mass
 333 of the selected data points and the origin. $|\vec{k}|$ is the absolute value of the degree of cur-
 334 vature of selected data points on Arai plots, put forward by Paterson (2011). A larger
 335 value of $|\vec{k}|$ indicates a more curved Arai plot. N is the minimum number of accepted
 336 specimens to calculate the sample-mean intensity. B_σ is the maximum accepted one-sigma
 337 standard deviation of sample-mean intensity, and $B_\sigma\%$ is the maximum accepted per-
 338 centage of B_σ relative to the sample-mean intensity; successful samples may not exceed
 339 both B_σ and $B_\sigma\%$.

340 **5 Results and Discussion**

341 A total of 36 out of 89 specimens passed the specimen-level CCRIT selection cri-
 342 teria. 6 out of 13 samples passed the sample-level selection criteria and yielded high-quality
 343 absolute paleointensity results. Estimated paleointensity results from all accepted sam-
 344 ples are listed in Table 1 and plotted as black symbols in Figure 5. Specimen-level pa-
 345 leointensity estimates and statistics for accepted samples are listed in Table 3. All sample-
 346 and specimen-level experimental results are archived in the MagIC database at <https://earthref.org/MagIC/19326>. Successful samples have a mean paleointensity value of 58.8
 347 μT with a standard deviation of 5.6 μT , which corresponds to a mean virtual axial dipole
 348 moment (VADM) of $86.3 \times 10^{21} \text{ Am}^2$ (ZAm^2) with a standard deviation of 4.93 ZAm^2 .
 349 The range of paleointensity values for the successful samples ranged from 49.5 to 68.0
 350 μT , corresponding to VADM values that range from 63.7 to 99.8 ZAm^2 (Figure 5).

352 Representative specimen results from the IZZI paleointensity experiment are shown
 353 in Figure 4 as NRM/TRM paleointensity plots and orthogonal demagnetization plots.
 354 Specimens in samples that passed CCRIT exhibit linear ratios between TRM acquired
 355 during in-field steps and NRM lost during associated zero-field steps, with reproducible
 356 pTRM checks (Figure 4). Specimens from the same sample that pass the paleointensity
 357 result selection generally have consistent behaviors, likely associated with their close min-
 358 eralogy assemblages. The majority of accepted specimens show single-component orthog-
 359 onal demagnetization plots (Figure 4), consistent with the interpretation that they have
 360 retained primary NRMs during cooling after eruption and have acquired minimum sec-
 361 ondary overprints.

362 Specimens that did not pass CCRIT (Figure 4) selection were rejected for display-
 363 ing non-linear TRM/NRM behavior over the course of the heating experiment. For ex-
 364 ample, specimen NA02-11Fi and NA92-59e (Figure 4) exhibit zigzagging and sagging Arai
 365 plot with failed pTRM checks beginning at 300°C and 510°C respectively. This is likely

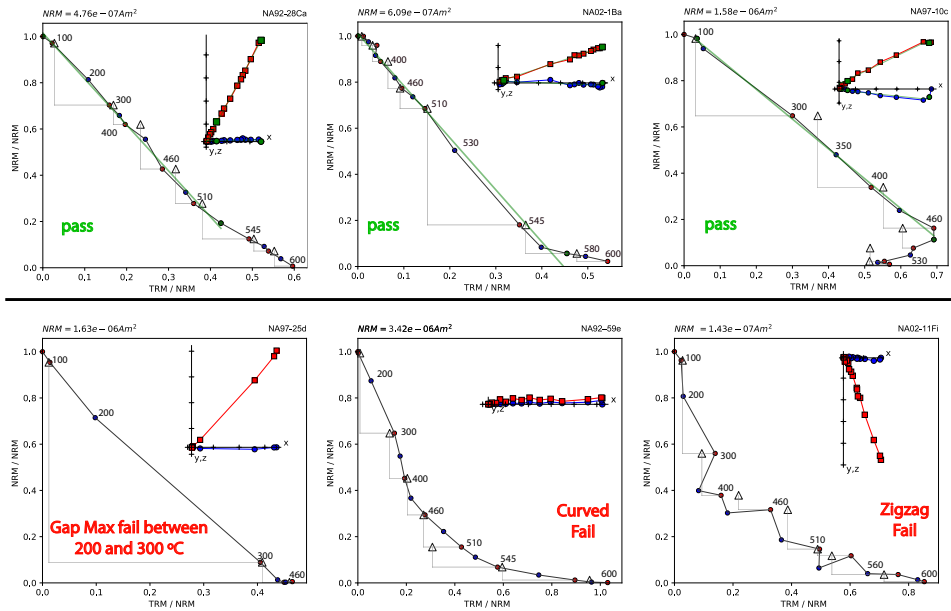


Figure 4. Representative specimen paleointensity Arai plots, showing normalized thermal remanent magnetization acquired during in-field heating steps plotted against normalized natural remanent magnetization removed during zero-field steps. In the Arai plots, temperature values are listed in degree Celsius, pTRM checks are shown as triangles, zero-field/in-field temperature steps are shown as red dots, in-field/zero-field steps are shown in blue. The green line is the least-squares component fit for selected temperature steps for specimens that pass the selection criteria. Inset orthogonal vector demagnetization diagrams (in specimen coordinates) show that the specimens have dominantly single component remanent magnetizations. Figures in the top row show typical paleointensity behavior of specimens with dominantly straight slope of NRM/TRM that pass the CCRIT selection criteria (Cromwell, Tauxe, Staudigel, & Ron, 2015); the bottom row shows typical behavior of specimens that fail the selection criteria.

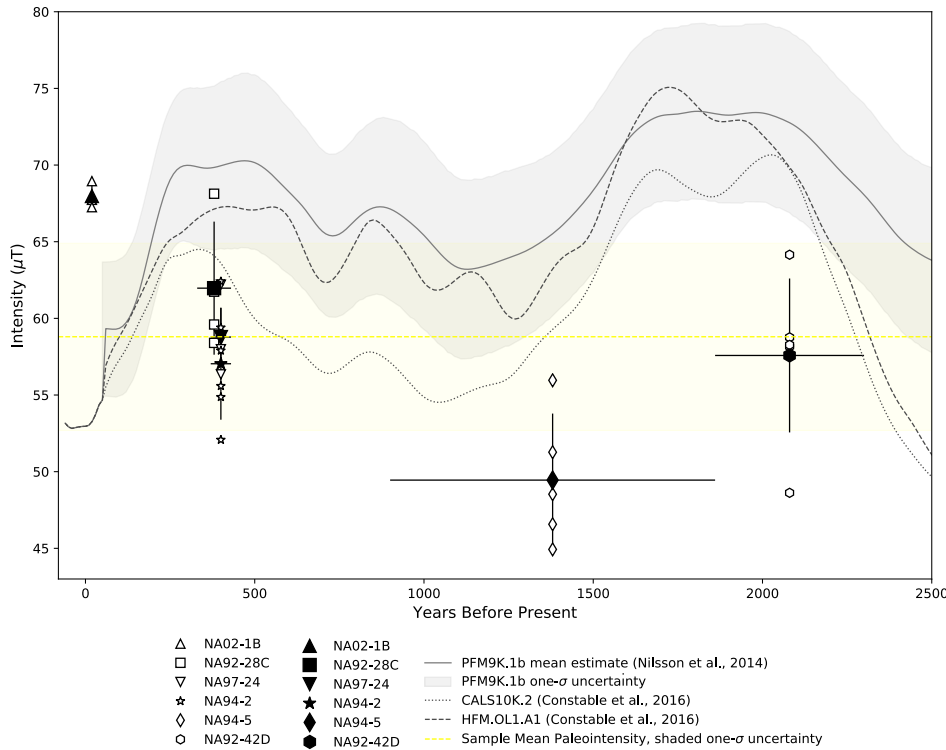


Figure 5. Summary of absolute paleointensity results from Aniakchak volcano with respect to predicted paleointensity values at Aniakchak volcano from global geomagnetic field models PFM9k.1b (Nilsson et al., 2014), CALS10k.2 (Constable et al., 2016), and HFM.OL1.A1 (Constable et al., 2016). The 1σ -uncertainty for model PFM9k.1b is shown as the grey area. Individual specimen paleointensity estimates (open symbols), sample-level average paleointensity results (closed symbols), together with one standard deviation uncertainties are plotted with respect to their estimated ages with uncertainties. Dashed yellow line and yellow rectangular area represents the mean paleointensity value of all samples ($58.8 \mu\text{T}$) and one standard deviation uncertainty. 1950 C.E. is used as zero years before present.

due to the contribution of vortex state or multi-domain (MD) magnetic grains within the specimens. Because vortex state and MD grains often unblock differently between in-field and zero-field steps (Tauxe & Staudigel, 2004; Yu et al., 2004), the alternating steps of in-field/zero-field (IZ) and zero-field/in-field (ZI) IZZI experimental protocol results in zigzagging or sagging of the Arai plot. Specimen NA97-25d has a linear Arai plot, but it fails the Gap Max criterion because of the great loss of NRM intensity between temperature steps 200°C and 300°C . In addition, the majority of the remanence in this specimen was removed after the 300°C heating step, indicating that the dominant magnetic carrier within the specimen is not likely stoichiometric single-domain magnetite and may be prone to secondary overprint.

Figure 5 summarizes individual specimen paleointensity results, sample-mean paleointensity results with one standard deviations, and locality-mean value of all successful samples, $58.8 \mu\text{T}$. Shown for comparison are the mean of the predicted surface intensities from global geomagnetic field model estimates at Aniakchak volcano for the last 2,500 yrs B.P. from models PFM9K.1b (Nilsson et al., 2014), CALS10k.2 (Constable et al., 2016), and HFMOL1.A1 (Constable et al., 2016). Specimens from samples that passed

382 the CCRIT selection criteria generally yield consistent specimen-level paleointensity es-
 383 timates. The overall sample-mean paleointensity estimates show a similar trend in field
 384 intensity as predicted by the geomagnetic field models, although the absolute paleoin-
 385 tensity values of the samples tends to be lower than that of the models (Figure 5). The
 386 sample and model intensities follow a high-low-high trend from *ca.* 2,300 to the present;
 387 they tend to peak between about 1,600 and 2,000 yrs B.P., decline to a low at about 1,300
 388 yrs B.P., and peak again between about 300 and 500 yrs B.P. .

389 The mean paleointensity estimate from sample NA92-42D which is from the sub-
 390 aqueous domes (unit Qd), is lower than the predicted values from the geomagnetic field
 391 models at *ca.* 2,100 yrs B.P. However, given its estimated age range between 1,860 yrs
 392 B.P. and 2,300 yrs B.P., an interpretation could be allowed that this sample was emplaced
 393 close to 2,300 yrs B.P. during the widespread pumice fall that was synchronous with or
 394 predates the emplacement of the subaqueous domes (Bacon et al., 2014).

395 If sample NA92-42D was emplaced close to 2,300 yrs B.P., its paleointensity value
 396 would be consistent with those predicted by models CALS10k.2 and HFMOL1.A1 and
 397 nearly within uncertainty of model PFM9K.1b (Figure 5).

398 Sample NA94-5 from Tuff Cone (unit Qtc) has a mean paleointensity estimate lower
 399 than what is predicted by all three geomagnetic field models (Figure 5). This sample has
 400 a broad estimated age range between 900 yrs B.P. and 1860 yrs B.P. If the age of this
 401 sample is closer to the minimum age estimate (as may be indicated by geochemical data,
 402 see "Stratigraphy and Age Constraints" section) then the range of paleointensity values
 403 of sample NA94-5 could be more consistent with the relatively low intensity values pre-
 404 dicted by the three geomagnetic field models at about 1,100 yrs. B.P. If this was the case,
 405 the paleointensity of sample NA94-5 would be consistent with the predicted decreasing
 406 trend in geomagnetic field intensity at Aniakchak volcano since the high between about
 407 1,600 and 2,000 yrs B.P., although the estimated absolute field intensity would under-
 408 estimate that predicted by the field models.

409 Samples NA94-2 and NA97-24 from Vent Mountain (unit Qvm), and sample NA92-
 410 28C from Half Cone (unit Qht) have similar estimated ages of 400 ± 30 and 380 ± 50 yrs
 411 B.P., respectively, and have indistinguishable estimated paleointensity values within the
 412 calculated uncertainty. (Table1; Figure 5). Despite having equivalent paleointensity es-
 413 timates, the mean value of the individual samples vary with respect to the predicted in-
 414 tensity of the geomagnetic field models. Samples NA94-2 and NA97-24 have lower es-
 415 timated intensities than all three field models, while the uncertainty bounds of sample
 416 NA92-28C are consistent with model CALS10k.2 and within the uncertainty of model
 417 PFM9K.1b. The paleointensity of samples NA94-2, NA97-24, and NA92-28C follow the
 418 predicted increasing trend in geomagnetic field intensity at Aniakchak volcano since about
 419 1,100 yrs B.P., although the absolute field intensity values from the samples are gener-
 420 ally lower than those predicted by the field models.

421 Sample NA02-1B from the 1931 C.E. tephra (unit Q3t) has a mean paleointensity
 422 estimate of $68.0 \mu\text{T}$, about $15 \mu\text{T}$ (25%) higher than the historical field strength at Ani-
 423 akchak volcano in 1931 C.E. ($53.2 \mu\text{T}$; estimated from IGRF12 using igrf.py, included
 424 as part of the PmagPy software package;(Tauxe et al., 2016)) and greater than the pre-
 425 dicted intensity from the geomagnetic field models (Table 1; Figure 5). The substantial
 426 overestimate of the historical field strength warrants additional consideration of the ex-
 427 perimental results for sample NA01-1B together with sample NA97-10, which was also
 428 emplaced during the 1931 C.E. eruption (part of the 1931 C.E. lava flow unit, Q3l). Arai
 429 plots of specimens from sample NA02-1B show hints of double-slope behavior that could
 430 be the result of unrecognized thermochemical alterations or post-emplacement heating,
 431 which could reduce the accuracy of the paleointensity interpretations from specimens that
 432 pass CCRIT (top left plot in Figure 4; Bowles et al. (2015)). The double-slope behav-
 433 iors in these specimens include a low temperature component between 0300°C and a higher

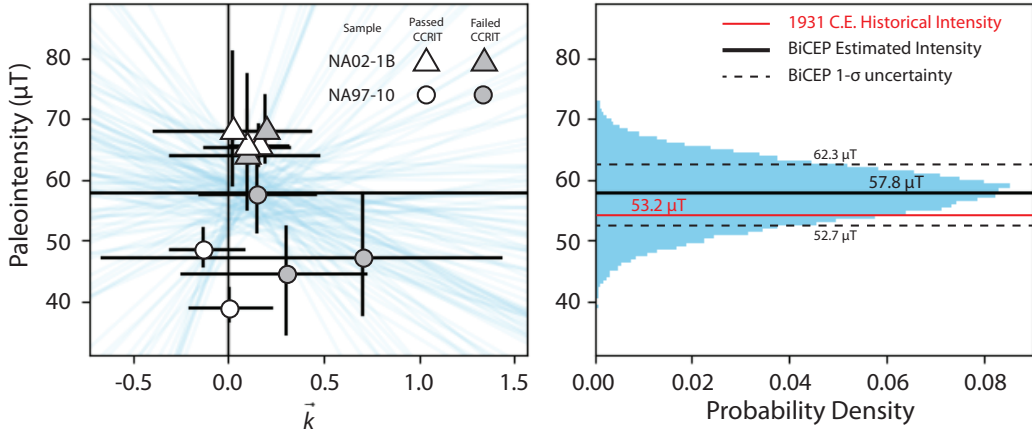


Figure 6. Estimated paleointensity results of the 1931 C.E. eruption from the Bias Corrected Estimation of Paleointensity (BiCEP) method (Cych et al., 2021). Left plot, estimated range of individual specimen paleointensity estimates relative to the estimated \vec{k} ; right plot, resulting estimate of 1931 C.E. field intensity and probability distribution.

temperature component between 350–560°C. After 560°C the specimens show signs of alteration as evidenced by failed pTRM checks (Figure 4). These specimens pass the CCRIT selection criteria despite observed non-linearity in the Arai plots, and yield consistent inter-sample paleointensity results (Figure 4; Table 1 and 3). Nevertheless, the possibility remains that the presence of MD grains or post-emplacement alterations could have led to erroneous paleointensity estimates.

Two specimens from sample NA97-10 pass the specimen-level CCRIT selection criteria and have estimated paleointensity values of 38.7 μT and 49.1 μT (Tables 1 and 3). However, sample NA97-10 failed the CCRIT sample-level criteria because a minimum of three specimens is required. The two successful specimens have linear Arai plots up to 460°C, after which they show signs of alteration as evidenced by failed pTRM checks (top right plot in Figure 4). Like the specimens from NA02-1B, the Arai plots of specimens from NA97-10 show hints of double-slope behavior at lower temperatures, as well as directional overprints in the Zijderveld diagrams. The successful specimen intensity values are about 4 to 15 μT lower than the historical field strength at Aniakchak volcano (53.2 μT) and at least 19 μT lower than the mean intensity for sample NA02-1B (68.0 μT). If the successful specimens from both 1931 C.E. samples were combined, the resulting mean paleointensity would be $58.3 \pm 13.7 \mu\text{T}$ and would have encompassed the historical field strength, although the resulting estimate would have failed the CCRIT B_σ and $B_{\sigma\%}$ sample-level criteria.

We apply the Bias Corrected Estimation of Paleointensity (BiCEP) method of Cych et al. (2021) as a different means of estimating the paleointensity and uncertainty from the 1931 C.E. samples. BiCEP is a Bayesian method which accounts for bias in paleointensity estimates of specimens, effectively weighting the paleointensity of different specimens using the curvature of the Arai plot as a metric of nonlinearity (where linearity is measured by the \vec{k} statistic) and a predictor of bias (Cych et al., 2021). Specimen paleointensity and bias are estimated using a range of selected temperature steps in the Arai plot. For the BiCEP calculation, we provided temperature steps for all specimens from samples NA02-1B and NA97-10, including those that failed the CCRIT selection criteria (Table 4). For the specimens that passed CCRIT, we used the temperature steps from the Thellier-GUI estimation (Table 3). For the specimens that failed CCRIT we

465 provided the temperature steps that represented the characteristic NRM/TRM of the
 466 paleointensity experiment, excluding low-temperature steps that deviate from the char-
 467 acteristic remanent magnetization direction on the Zijderveld plots, and high-temperature
 468 steps where thermochemical alteration occurred as evidenced by failed pTRM checks in
 469 the Arai plot.

470 The BiCEP estimation using all specimens from samples NA02-1B and NA97-10
 471 generated “B-Grade” results (Cych et al., 2021), which are shown in Figure 6. The range
 472 of individual specimen paleointensity estimates relative to the range of estimated \vec{k} is
 473 shown on the left plot of Figure 6. The distribution and range of estimates on the plot
 474 is typical to the BiCEP calculation when the specimen-level experimental results have
 475 a range of quality and linearity in their Arai plot. The resulting probability distribution
 476 of estimated paleointensities is shown on the right plot of Figure 6. The median pale-
 477 ointensity value from the probability distribution was $57.8 \mu\text{T}$, about $4.5\mu\text{T}$ higher than
 478 the 1931 C.E. historical field intensity (Figure 6). The calculated $1-\sigma$ uncertainty range
 479 from BiCEP was $52.7\mu\text{T}$ and $62.3\mu\text{T}$. The resulting paleointensity estimate from BiCEP
 480 is within the $1-\sigma$ uncertainty range of the historical field strength for 1931 C.E. The Bi-
 481 CEP method provides a reasonable estimate and associated uncertainty of the 1931 C.E.
 482 field intensity at Aniakchak volcano based on the experimental results from the avail-
 483 able samples. The inter-sample variability between the 1931 C.E. samples indicates that
 484 there may be rock magnetic, mineralogical, and (or) post-emplacement effects that af-
 485 fected the viability of the paleointensity experiment, warranting further investigation of
 486 these samples and additional sample collection.

487 6 Conclusion

488 In this study we report high-quality paleointensity results for the past 2,300 years
 489 from rapidly cooled, glassy volcanic material from Aniakchak volcano, Alaska, USA. Six
 490 samples pass the CCRIT selection criteria and provide paleointensity estimates. These
 491 new paleointensity results are a valuable contribution to the mid- to high-northern lat-
 492 itude paleomagnetic dataset for North America. Although our sample-mean paleointen-
 493 sities are generally lower than predicted model intensities, paleointensity results for five
 494 samples are generally consistent with predicted variability in field strengths from global
 495 geomagnetic field models, considering age and experimental uncertainties. One sample
 496 for the historical 1931 C.E. eruption passed the CCRIT selection criteria and had robust
 497 inter-specimen consistency. However it yielded a paleointensity result about $15 \mu\text{T}$ higher
 498 than the historical field strength. Further analyses using a Bayesian estimation method
 499 of specimens from this sample and another sample from the 1931 C.E. eruption yielded
 500 a probability estimate with $1-\sigma$ uncertainty that is consistent with the historical field strength.
 501 Further investigation of samples from the 1931 C.E. eruption is warranted to investigate
 502 potential rock magnetic, mineralogical, and (or) post-emplacement effects on the pale-
 503 ointensity results. Overall, the paleointensity results from Aniakchak volcano help pro-
 504 vide new spatial and temporal coverage for future geomagnetic field models. Additional
 505 sampling of glassy volcanic materials paired with more precise age controls in future stud-
 506 ies at Aniakchak volcano and other volcanoes along the Alaska-Aleutian arc will further
 507 constrain estimates of geomagnetic field behavior in North America.

Table 1: Table of location information, field observations, estimated ages, absolute paleointensity results, and calculated VADM values for all samples. *Lat* and *Lon* are degrees latitude (north) and longitude (east) based on datum NAD83. *Age* is interpreted sample age (years before calendar year 1950 C.E.) and age uncertainty (years). *Unit* is the map unit from Figure 1. *nn* is number of accepted specimens for successful samples, and *n* is total specimens measured. *B_F* is the estimated ancient field strength in μT , *B_F σ* is the standard deviation of *B_F*. VADM (virtual axial dipole moment) and VADM σ values are in Am^2 . *Sample Location and Description* are descriptions of the field locality and physical sample.

Sample	Lat	Lon	Age	Unit	nn/n	<i>B_F</i>	<i>B_Fσ</i>	VADM	VADM σ	Sample Location and Description
NA92-42D	56.9026	-158.2243	1,860±2,300	Qd	6/7	57.6	5.02	8.45E+22	7.37E+21	1931 Main Crater, west wall;
NA02-10G	56.9015	-158.2244	1,860±2,300	Qd	-/7	-	-	-	-	pre-Half Cone, dense, gray, sparsely porphyritic lava flow, platy jointing
NA94-5	56.8951	-158.0882	900±1,860	Qtc?	5/9	49.5	4.34	7.26E+22	6.37E+21	1931 Main Crater, west wall;
NA94-2	56.8793	-158.1358	400±30	Qvm	6/6	57.0	3.65	8.37E+22	5.36E+21	dense, gray lava flow with platy jointing high in west 1931 crater wall
NA97-24	56.88	-158.134	400±30	Qvm	6/7	58.8	1.91	8.63E+22	2.80E+21	Lower flow terrace below big maar;
NA97-25	56.8859	-158.1248	400±30	Qvm	-/6	-	-	-	-	older lava flow near The Gates; possible Windy Cone source
NA93-100A	56.8939	-158.1294	840±900	Qvm	2/7	-	-	-	-	New Cone rim, southeast flank of Vent Mountain;
NA92-28C	56.9076	-158.2019	380±50	Qht	4/6	62.0	4.34	9.09E+22	6.37E+21	dark brown, scoraceous, porphyritic pumice
NA92-59	56.895	-158.1686	380±50	Qht	2/6	-	-	-	-	East rim New Cone crater;
NA02-10F	56.9015	-158.2244	380±50	Qht?	-/9	-	-	-	-	New Cone agglutinate
NA02-11F	56.9066	-158.2132	> 840±40	Qhc?	-/9	-	-	-	-	Alluvial flat east of Vent Mountain;
NA02-1B	56.8893	-158.191	1931 C.E.	Q31t?	3/5	68.0	0.88	9.98E+22	1.29E+21	Vent Mountain lava, possibly related to New Cone
NA97-10	56.908	-158.21	1931 C.E.	Q31	2/5	-	-	-	-	East base of Vent Mountain;
										Vent Mountain lava younger than tuff cones, at base of tephra section
										Half Cone agglutinate
										North base Vent Mountain;
										Half Cone agglutinate
										1931 Main Crater west wall;
										black agglutinate half cone?
										1931 Main Crater north wall;
										welded volcaniclastic
										Between Blocky Cone and the base of Vent Mountain;
										1931 scoria
										1931 Main Crater floor near base of north wall;
										1931 spatter-fed lava flow

Table 2. Specimen- and sample-level criteria for the CCRIT (Cromwell, Tauxe, & Halldórsson, 2015) selection method (*SCAT* criterion uses a $\beta_{threshold}$ value of 0.1). Refer to the “Selection Criteria” section or Paterson et al. (2014) for descriptions of each statistic.

CCRIT Paleointensity Selection Criteria										
<i>SCAT</i>	<i>FRAC</i>	<i>Gap Max</i>	<i>Specimen</i>			$ \vec{k} $	<i>N</i>	<i>Sample</i>		
			β	MAD_{free}	<i>DANG</i>			B_σ	$B_\sigma\ %$	
PASS	≥ 0.78	≤ 0.60	≤ 0.10	$\leq 5.0^\circ$	$\leq 10.0^\circ$	≤ 0.164	$ \geq 3$	$\leq 4\ \mu\text{T}$	$\leq 10\ %$	

Table 3: Summary table of specimen-level paleointensity experiment results. Paleointensity results and selection criteria statistics are listed for specimens that passed the CCRIT selection criteria. Specimen and Sample are paleomagnetic specimens and their respective samples. B_F is the measured intensity in microTesla, T_{low} and T_{high} are lower and upper temperature bounds (degrees Celsius) used to calculate intensity, and n and n_{pTRM} are the number of temperature steps and pTRM checks used in that same calculation. SCAT, FRAC, Gap Max, β , MAD_{free}, DANG, and $|\vec{k}|$ are statistics used to determine specimen reliability. See Selection Criteria section for a description of all statistics, and Table 2 for selection criteria.

Specimen	Sample	B_F	T_{low}	T_{high}	n	n_{pTRM}	SCAT	FRAC	Gap Max	β	MAD_{free}	DANG	$ \vec{k} $
NA92-42Da	NA92-42D	58.76	0	400	6	2	PASS	0.92	0.46	0.08	3.6	1.56	-0.02
NA92-42Db	NA92-42D	58.16	100	400	5	2	PASS	0.88	0.52	0.06	2.02	2.37	-0.08
NA92-42Dc	NA92-42D	58.27	100	400	5	2	PASS	0.89	0.51	0.05	2.99	3.01	0
NA92-42Dd	NA92-42D	64.15	0	430	7	2	PASS	0.95	0.48	0.04	1.76	1.6	0.04
NA92-42De	NA92-42D	57.53	0	400	6	2	PASS	0.92	0.46	0.05	2.24	2.39	0.08
NA92-42Df	NA92-42D	48.62	100	460	7	3	PASS	0.92	0.55	0.04	3.92	2.37	-0.1
NA92-42Dg	NA92-42D												
NA02-10Ca	NA02-10G												
NA02-10Gb	NA02-10G												
NA02-10Gc	NA02-10G												
NA02-10Gd	NA02-10G												
NA02-10Ge	NA02-10G												
NA02-10Gf	NA02-10G												
NA02-10Gg	NA02-10G												
NA94-5a	NA94-5												
NA94-5b	NA94-5	48.53	0	430	7	2	PASS	0.81	0.37	0.05	4.88	4.88	0.16
NA94-5c	NA94-5	46.57	0	430	7	2	PASS	0.79	0.34	0.06	3.56	1.39	0
NA94-5d	NA94-5												
NA94-5e	NA94-5												
NA94-5f	NA94-5	51.27	0	430	7	2	PASS	0.85	0.35	0.06	3.17	2.29	0.12
NA94-5g	NA94-5												
NA94-5h	NA94-5	55.96	200	560	11	5	PASS	0.89	0.21	0.04	4.96	1.22	0
NA94-5i	NA94-5	44.93	200	580	12	6	PASS	0.84	0.14	0.04	2.86	0.97	-0.04
NA94-2a	NA94-2	55.59	100	460	7	3	PASS	0.95	0.59	0.02	1.86	0.81	0
NA94-2b	NA94-2	57.9	0	490	9	3	PASS	0.96	0.52	0.05	2.89	0.93	0.15
NA94-2c	NA94-2	59.4	0	510	10	4	PASS	0.99	0.54	0.03	1.54	0.79	0.16

NA94-2d	NA94-2	54.87	0	460	8	3	PASS	0.97	0.46	0.04	1.44	1.1	-0.04	
NA94-2e	NA94-2	52.08	100	460	7	3	PASS	0.95	0.59	0.02	1.54	0.99	0.09	
NA94-2f	NA94-2	62.41	0	490	9	3	PASS	0.98	0.57	0.03	1.73	0.8	-0.05	
NA97-24a	NA97-24	58.84	350	580	10	6	PASS	0.82	0.28	0.03	3.8	0.26	0	
NA97-24b	NA97-24	62.2	0	580	14	6	PASS	1	0.14	0.03	2.52	0.33	0.1	
NA97-24c	NA97-24	58.59	0	545	12	5	PASS	0.78	0.41	0.04	4.23	0.76	0	
NA97-24d	NA97-24	57.99	200	545	10	5	PASS	0.79	0.31	0.03	4.15	2.43	0	
NA97-24e	NA97-24	56.35	200	560	11	5	PASS	0.96	0.39	0.04	3.92	0.79	0.16	
NA97-24f	NA97-24	58.72	0	545	12	5	PASS	0.88	0.38	0.03	3.45	1.8	0	
NA97-25g	NA97-25	NA97-25	NA97-25	NA97-25	NA97-25	NA97-25	NA97-25	NA97-25	NA97-25	NA97-25	NA97-25	NA97-25	NA97-25	
NA97-25a	NA97-25b	NA97-25c	NA97-25d	NA97-25e	NA97-25f	NA97-25f	NA93-100Aa	NA93-100Ab	NA93-100Ac	NA93-100Ad	NA93-100Ae	NA93-100Af	NA93-100Ag	
NA93-100Aa	NA93-100Ab	NA93-100A	42.6	100	510	9	4	PASS	0.87	0.34	0.02	4	6	0.002
NA93-100Ac	NA93-100A	42.8	0	460	8	3	PASS	0.85	0.38	0.05	3.3	8.7	0.065	
NA93-100Ad	NA93-100A	NA93-100A	NA93-100A	NA93-100A	NA93-100A	NA93-100A	NA93-100A	NA92-28Ca	NA92-28Cb	NA92-28Cc	NA92-28Cd	NA92-28Ce	NA92-28Cf	NA92-28Cf
NA93-100Ae	NA93-100Af	NA93-100Ag	NA93-100A	NA93-100A	NA93-100A	NA93-100A	NA93-100A	NA92-28C	NA92-28C	NA92-28C	NA92-28C	NA92-28C	NA92-28C	NA92-28C
NA93-100Af	NA93-100Ag	NA92-28C	59.6	0	530	11	4	PASS	0.81	0.19	0.02	1.82	0.96	-0.02
NA92-28Ca	NA92-28Cb	NA92-28Cc	NA92-28Cd	NA92-28Ce	NA92-28Cf	NA92-28Cf	NA92-28Cf	58.4	0	530	11	4	NA92-59a	NA92-59b
NA92-28Cb	NA92-28Cc	NA92-28Cd	NA92-28Ce	NA92-28Cf	NA92-59a	NA92-59b	NA92-59b	61.74	0	560	13	5	NA92-59c	NA92-59d
NA92-28Cc	NA92-28Cd	NA92-28Ce	NA92-28Cf	NA92-28Cf	NA92-59a	NA92-59b	NA92-59b	68.13	0	560	13	5	NA92-59c	NA92-59d
NA92-28Cd	NA92-28Ce	NA92-28Cf	NA92-28Cf	NA92-28Cf	NA92-59a	NA92-59b	NA92-59b	73.5	100	490	8	3	NA92-59c	NA92-59d

Table 4: Summary table of estimated paleointensity results of the 1931 C.E. eruption from the Bias Corrected Estimation of Paleointensity (BiCEP) method (Cych et al., 2021). Specimen and Sample are paleomagnetic specimens and their respective samples. B_F is the estimated intensity in microTesla, $B_F\text{-}Min$ and $B_F\text{-}Max$ are 95% confidence interval minimum and maximum estimates of paleointensity. T_{Low} and T_{High} are lower and upper temperature bounds (degrees Celsius) used in the BiCEP estimation. $\vec{k}\text{-}Min$ and $\vec{k}\text{-}Max$ are the minimum and maximum range estimates of the \vec{k} statistic. The resulting paleointensity estimate for the 1931 C.E. eruption is listed with 1σ uncertainty range.

Specimen	Sample	B_F	$B_F\text{-}Min$	$B_F\text{-}Max$	T_{Low}	T_{High}	\vec{k}	$\vec{k}\text{-}Min$	$\vec{k}\text{-}Max$
NA02-1Ba	NA02-1B	65.4	62.3	69.1	0	570	0.157	0.002	0.309
NA02-1Bb	NA02-1B	67.8	59.1	81	200	560	0.021	-0.389	0.421
NA02-1Bc	NA02-1B	65.4	60.6	71.3	0	560	0.1	-0.122	0.317
NA02-1Bd	NA02-1B	67.9	62.8	73.8	200	560	0.19	-0.058	0.429
NA02-1Be	NA02-1B	63.8	55.2	77.2	100	560	0.098	-0.298	0.477
NA97-10a	NA97-10	44.5	34.6	52.1	300	490	0.304	-0.244	0.719
NA97-10b	NA97-10	57.6	51.5	63	300	570	0.153	-0.148	0.453
NA97-10c	NA97-10	38.9	36.6	42.1	100	490	0.003	-0.199	0.225
NA97-10d	NA97-10	47.1	37.9	57.8	300	460	0.704	-0.658	1.424
NA97-10e	NA97-10	48.5	45.8	51.9	0	430	-0.13	-0.298	0.079
1931 C.E.		57.8	52.7	62.3					

508 **Acknowledgments**

509 We thank Scott Bogue for his support throughout this grant, and Brendan Cych for help
 510 with the BiCEP result interpretations. We thank Michelle Coombs and the staff at the
 511 USGS Alaska Volcano Observatory and the Geologic Materials Center in Anchorage, Alaska
 512 for providing access to sample material. Thanks to Jordan Bretthauer and Cole Valentino
 513 for their work in collecting sample material from the Alaska Volcano Observatory archives.
 514 We thank two anonymous reviewers for their constructive reviews, and the editorial staff
 515 at the journal. All measurement-level data and results are archived in the MagIC database
 516 and can be accessed at <https://earthref.org/MagIC/19326>; scripts used to evaluate
 517 the paleointensity data and to generate selected figures are archived at https://github.com/duserzym/2021_Aniakchak. Support was provided through National Science Foun-
 518 dation grant EAR1520788 to G. Cromwell.

520 **References**

- 521 Arai, Y. (1963). Secular variation in intensity of the past geomagnetic field. *M.Sc. thesis, University of Tokyo, Tokyo, Japan.*
- 522 Bacon, C. R., Neal, C. A., Miller, T. P., McGimsey, R. G., & Nye, C. J. (2014). Postglacial eruptive history, geochemistry, and recent seismicity of Aniakchak volcano, Alaska Peninsula. *US Geological Survey Professional Paper 1810*. doi: 10.3133/pp1810
- 523 Barletta, F., St-Onge, G., Channell, J. E., Rochon, A., Polyak, L., & Darby, D. (2008). High-resolution paleomagnetic secular variation and relative paleointensity records from the western Canadian Arctic: implication for Holocene stratigraphy and geomagnetic field behaviour. This article is one of a series of papers published in this Special Issue on the theme Polar Climate Stability Network. GEOTOP Contribution 2008-0024. *Canadian Journal of Earth Sciences*, 45(11), 1265–1281. doi: 10.1139/e08-039
- 524 Begét, J., Mason, O., & Anderson, P. (1992). Age, Extent and Climatic Significance of the c. 3400 BP Aniakchak Tephra, Western Alaska, USA. *The Holocene*, 2(1), 51–56. doi: 10.1177/095968369200200106
- 525 Bingham, D. K., & Stone, D. B. (1972). Palaeosecular Variation of the Geomagnetic Field in the Aleutian Islands, Alaska. *Geophysical Journal International*, 28(4), 317–335. doi: 10.1111/j.1365-246x.1972.tb06796.x
- 526 Bowles, J. A., Gee, J. S., Jackson, M. J., & Avery, M. S. (2015). Geomagnetic paleointensity in historical pyroclastic density currents: Testing the effects of emplacement temperature and postemplacement alteration. *Geochemistry, Geophysics, Geosystems*, 16(10), 3607–3625. doi: 10.1002/2015gc005910
- 527 Brown, M. C., Donadini, F., Korte, M., Nilsson, A., Korhonen, K., Lodge, A., ... Constable, C. G. (2015). Geomagia50.v3: 1. general structure and modifications to the archeological and volcanic database. *Earth, Planets and Space*, 67(1). doi: 10.1186/s40623-015-0232-0
- 528 Brown, M. C., Donadini, F., Nilsson, A., Panovska, S., Frank, U., Korhonen, K., ... Constable, C. G. (2015). Geomagia50.v3: 2. a new paleomagnetic database for lake and marine sediments. *Earth, Planets and Space*, 67(1). doi: 10.1186/s40623-015-0233-z
- 529 Cai, S., Tauxe, L., & Cromwell, G. (2017). Paleointensity From Subaerial Basaltic Glasses From the Second Hawaii Scientific Drilling Project (HSDP2) Core and Implications for Possible Bias in Data From Lava Flow Interiors. *Journal of Geophysical Research: Solid Earth*, 122(11), 8664–8674. doi: 10.1002/2017jb014683
- 530 Coe, R. S. (1967). The Determination of Paleo-Intensities of the Earth's Magnetic Field with Emphasis on Mechanisms which Could Cause Non-ideal Behavior in Thellier's Method. *Journal of geomagnetism and geoelectricity*, 19(3), 157–179. doi: 10.5636/jgg.19.157

- 561 Coe, R. S., Zhao, X., Lyons, J. J., Pluhar, C. J., & Mankinen, E. A. (2000). Revis-
 562 iting the 1964 collection of Nuvivak lava flows. *EOS Trans. AGU*, *81*(48), Fall
 563 Meeting Suppl., Abstract GP62A-06.
- 564 Constable, C., Korte, M., & Panovska, S. (2016). Persistent high paleosecular varia-
 565 tion activity in southern hemisphere for at least 10000 years. *Earth and Plane-
 566 tary Science Letters*, *453*, 78–86. doi: 10.1016/j.epsl.2016.08.015
- 567 Cromwell, G., Tauxe, L., & Halldórsson, S. A. (2015). New paleointensity results
 568 from rapidly cooled Icelandic lavas: Implications for Arctic geomagnetic field
 569 strength. *Journal of Geophysical Research: Solid Earth*, *120*(5), 2913–2934.
 570 doi: 10.1002/2014jb011828
- 571 Cromwell, G., Tauxe, L., Staudigel, H., & Ron, H. (2015). Paleointensity estimates
 572 from historic and modern Hawaiian lava flows using glassy basalt as a primary
 573 source material. *Physics of the Earth and Planetary Interiors*, *241*, 44–56. doi:
 574 10.1016/j.pepi.2014.12.007
- 575 Cromwell, G., Trusdell, F., Tauxe, L., Staudigel, H., & Ron, H. (2018). Holocene
 576 Paleointensity of the Island of Hawai‘i From Glassy Volcanics. *Geochemistry,
 577 Geophysics, Geosystems*, *19*(9), 3224–3245. doi: 10.1002/2017gc006927
- 578 Cych, B., Morzfeld, M., & Tauxe, L. (2021). Bias corrected estimation of pa-
 579 leointensity (BiCEP): An improved methodology for obtaining paleoin-
 580 tensity estimates. *Geochemistry, Geophysics, Geosystems*, *22*(8). doi:
 581 10.1029/2021gc009755
- 582 Dreher, S. T., Eichelberger, J. C., & Larsen, J. F. (2005). The Petrology and Geo-
 583 chemistry of the Aniakchak Caldera-forming Ignimbrite, Aleutian Arc, Alaska.
 584 *Journal of Petrology*, *46*(9), 1747–1768. doi: 10.1093/petrology/egi032
- 585 Dunlop, D. J. (2005). Linear and nonlinear Thellier paleointensity behav-
 586 ior of natural minerals. *Journal of Geophysical Research*, *110*(B1). doi:
 587 10.1029/2004jb003095
- 588 Geologic Materials Center. (2015). Alaska Department of Natural Resources, Di-
 589 vision of Geological and Geophysical Surveys, Anchorage, Alaska. Retrieved
 590 from <https://maps.dggs.alaska.gov/gmc/>
- 591 George, R. (2004). Chemical versus Temporal Controls on the Evolution of Tholei-
 592 itic and Calc-alkaline Magmas at Two Volcanoes in the Alaska-Aleutian Arc.
 593 *Journal of Petrology*, *45*(1), 203–219. doi: 10.1093/petrology/egg086
- 594 Hillhouse, J. W., & Grommé, C. S. (1980). Paleomagnetism of the Triassic Hound
 595 Island Volcanics, Alexander Terrane, southeastern Alaska. *Journal of Geophys-
 596 ical Research*, *85*(B5), 2594. doi: 10.1029/jb085ib05p02594
- 597 Hubbard, B. (1931). A world inside a mountain. *National Geographic Society*, *60*(3),
 598 319–345.
- 599 Jicha, B. R., Scholl, D. W., Singer, B. S., Yogodzinski, G. M., & Kay, S. M. (2006).
 600 Revised age of Aleutian Island Arc formation implies high rate of magma
 601 production. *Geology*, *34*(8), 661. doi: 10.1130/g22433.1
- 602 Johnson, C. L., Constable, C. G., Tauxe, L., Barendregt, R., Brown, L. L., Coe,
 603 R. S., ... et al. (2008). Recent investigations of the 0–5 Ma geomagnetic field
 604 recorded by lava flows. *Geochemistry, Geophysics, Geosystems*, *9*(4), 31. doi:
 605 10.1029/2007gc001696
- 606 Korte, M., & Constable, C. (2011). Improving geomagnetic field reconstructions for
 607 0–3ka. *Physics of the Earth and Planetary Interiors*, *188*(3–4), 247–259. doi:
 608 10.1016/j.pepi.2011.06.017
- 609 Korte, M., Constable, C., Donadini, F., & Holme, R. (2011). Reconstructing the
 610 Holocene geomagnetic field. *Earth and Planetary Science Letters*, *312*(3–4),
 611 497–505. doi: 10.1016/j.epsl.2011.10.031
- 612 Korte, M., Donadini, F., & Constable, C. G. (2009). Geomagnetic field for 0–3 ka: 2.
 613 A new series of time-varying global models. *Geochemistry, Geophysics, Geosys-
 614 tems*, *10*(6). doi: 10.1029/2008gc002297
- 615 Lisé-Pronovost, A., St-Onge, G., Brachfeld, S., Barletta, F., & Darby, D. (2009).

- 616 Paleomagnetic constraints on the Holocene stratigraphy of the Arctic
 617 Alaskan margin. *Global and Planetary Change*, 68(1-2), 85–99. doi:
 618 10.1016/j.gloplacha.2009.03.015
- 619 McGimsey, R., Waythomas, C., & Neal, C. (1994). High stand and catastrophic
 620 draining of intracaldera Surprise Lake, Aniakchak Volcano, Alaska. *US Geological Survey Bulletin* 2109, 59–71. doi: 10.3133/70180217
- 622 Miller, T. P., & Smith, R. L. (1977). Spectacular mobility of ash flows around Ani-
 623 akchak and Fisher calderas, Alaska. *Geology*, 5(3), 173. doi: 10.1130/0091-
 624 -7613(1977)5<173:smoafa>2.0.co;2
- 625 Miller, T. P., & Smith, R. L. (1987). Late Quaternary caldera-forming eruptions
 626 in the eastern Aleutian arc, Alaska. *Geology*, 15(5), 434. doi: 10.1130/0091-
 627 -7613(1987)15<434:lqceit>2.0.co;2
- 628 Neal, C., McGimsey, R., Braitseva, O., Miller, T., Eichelberger, J., & Nye, C.
 629 (1992). Postcaldera eruptive history of Aniakchak caldera, Alaska. *Eos*,
 630 73, 645.
- 631 Neal, C. A., McGimsey, R. G., Miller, T. P., Riehle, J. R., Waythomas, C. F., et
 632 al. (2001). Preliminary Volcano-Hazard Assessment for Aniakchak Volcano,
 633 Alaska. *US Geological Survey Open-File Report 00-519*, 35.
- 634 Nicholson, R. S., Gardner, J. E., & Neal, C. A. (2011). Variations in eruption style
 635 during the 1931A.D. eruption of Aniakchak volcano, Alaska. *Journal of Vol-
 636 canology and Geothermal Research*, 207(3-4), 69–82. doi: 10.1016/j.jvolgeores
 637 .2011.08.002
- 638 Nilsson, A., Holme, R., Korte, M., Suttie, N., & Hill, M. (2014). Reconstructing
 639 Holocene geomagnetic field variation: new methods, models and implications.
 640 *Geophysical Journal International*, 198(1), 229–248. doi: 10.1093/gji/ggu120
- 641 Packer, D. R., & Stone, D. B. (1974). Paleomagnetism of Jurassic Rocks from
 642 Southern Alaska, and the Tectonic Implications. *Canadian Journal of Earth
 643 Sciences*, 11(7), 976–997. doi: 10.1139/e74-095
- 644 Paterson, G. A. (2011). A simple test for the presence of multidomain behavior
 645 during paleointensity experiments. *Journal of Geophysical Research*, 116(B10).
 646 doi: 10.1029/2011jb008369
- 647 Paterson, G. A., Tauxe, L., Biggin, A. J., Shaar, R., & Jonestrask, L. C. (2014). On
 648 improving the selection of Thellier-type paleointensity data. *Geochemistry,
 649 Geophysics, Geosystems*, 15(4), 1180–1192. doi: 10.1002/2013gc005135
- 650 Pavón-Carrasco, F. J., Osete, M. L., Torta, J. M., & De Santis, A. (2014). A
 651 geomagnetic field model for the Holocene based on archaeomagnetic and
 652 lava flow data. *Earth and Planetary Science Letters*, 388, 98–109. doi:
 653 10.1016/j.epsl.2013.11.046
- 654 Pearce, C., Varhelyi, A., Wastegård, S., Muschitiello, F., Barrientos, N., ORegan,
 655 M., ... Jakobsson, M. (2017). The 3.6ka Aniakchak tephra in the Arctic
 656 Ocean: a constraint on the Holocene radiocarbon reservoir age in the Chukchi
 657 Sea. *Climate of the Past*, 13(4), 303–316. doi: 10.5194/cp-13-303-2017
- 658 Shaar, R., & Tauxe, L. (2013). Thellier GUI: An integrated tool for analyzing pa-
 659 leointensity data from Thellier-type experiments. *Geochemistry, Geophysics,
 660 Geosystems*, 14(3), 677–692. doi: 10.1002/ggpe.20062
- 661 Smith, W. R. (1925). Aniakchak Crater, Alaska Peninsula. *U.S. Geological Survey
 662 Professional Paper 132-J*. doi: 10.3133/pp132j
- 663 Stamatakos, J. A., Trop, J. M., & Ridgway, K. D. (2001). Late Cretaceous pa-
 664 leogeography of Wrangellia: Paleomagnetism of the MacColl Ridge For-
 665 mation, southern Alaska, revisited. *Geology*, 29(10), 947. doi: 10.1130/
 666 0091-7613(2001)029<0947:lcpowp>2.0.co;2
- 667 Stone, D. B., & Layer, P. W. (2006). Paleosecular variation and GAD studies of
 668 0-2 Ma flow sequences from the Aleutian Islands, Alaska. *Geochemistry, Geo-
 669 physics, Geosystems*, 7(4), n/a–n/a. doi: 10.1029/2005gc001007
- 670 Stone, D. B., & Packer, D. R. (1979). Paleomagnetic data from the Alaska Penin-

- 671 sula. *Geological Society of America Bulletin*, 90(6), 545. doi: 10.1130/0016
672 -7606(1979)90<545:pdftap>2.0.co;2
- 673 Symonds, R. B., Poreda, R. J., Evans, W. C., Janik, C. J., & Ritchie, B. E. (2003).
674 Mantle and crustal sources of carbon, nitrogen, and noble gases in Cascade-
675 Range and Aleutian-Arc volcanic gases. *US Geological Survey Open-File
Report 03-436*, 26.
- 676 Tauxe, L., & Kent, D. V. (2004). A Simplified Statistical Model for the Geomagnetic
677 Field and the Detection of Shallow Bias in Paleomagnetic Inclinations: was the
678 Ancient Magnetic Field Dipolar? *Geophysical Monograph Series*, 101–115. doi:
680 10.1029/145gm08
- 681 Tauxe, L., Shaar, R., Jonestrask, L., Swanson-Hysell, N. L., Minnett, R., Koppers,
682 A. A. P., ... Fairchild, L. (2016). PmagPy: Software package for paleomag-
683 netic data analysis and a bridge to the Magnetics Information Consortium
684 (MagIC) Database. *Geochemistry, Geophysics, Geosystems*, 17(6), 2450–2463.
685 doi: 10.1002/2016gc006307
- 686 Tauxe, L., & Staudigel, H. (2004). Strength of the geomagnetic field in the Cre-
687 taceous Normal Superchron: New data from submarine basaltic glass of
688 the Troodos Ophiolite. *Geochemistry, Geophysics, Geosystems*, 5(2). doi:
689 10.1029/2003gc000635
- 690 Thrupp, G. A., & Coe, R. S. (1986). Early Tertiary paleomagnetic evidence and
691 the displacement of southern Alaska. *Geology*, 14(3), 213. doi: 10.1130/0091
692 -7613(1986)14<213:etpeat>2.0.co;2
- 693 VanderHoek, R. (2009). The role of ecological barriers in the development of cultural
694 boundaries during the later Holocene of the central Alaska Peninsula. *Ph.D.
dissertation*.
- 695 VanderHoek, R., & Myron, R. (2004). An archaeological overview and assessment of
696 Aniakchak National Monument and Preserve. *U.S. National Park Service Re-
697 search/ Resources Management Report, AR/CRR-2004-47*.
- 698 Yu, Y., Tauxe, L., & Genevey, A. (2004). Toward an optimal geomagnetic field in-
699 tensity determination technique. *Geochemistry, Geophysics, Geosystems*, 5(2),
700 n/a–n/a. doi: 10.1029/2003gc000630